THE ASTROPHYSICAL JOURNAL, 395:L9–L12, 1992 August 10

ULTRAVIOLET IMAGING TELESCOPE OBSERVATIONS OF THE CYGNUS LOOP

ROBERT H. CORNETT,[1] EDWARD B. JENKINS,[2] RALPH C. BOHLIN,[3] KWANG-PING CHENG,[4] THEODORE R. GULL,[4]
ROBERT W. O'CONNELL,[5] ROBERT A. R. PARKER,[6] MORTON S. ROBERTS,[7] ANDREW M. SMITH,[4]
ERIC P. SMITH,[4] AND THEODORE P. STECHER[4]
Received 1992 March 31; accepted 1992 May 18

ABSTRACT

Ultraviolet images of a 40′ field in the northeast part of the Cygnus Loop were made by the Ultraviolet Imaging Telescope (UIT) during the *Astro-1* mission in 1990 December. This *Letter* compares the longest far-UV (B5) exposure with ground-based and X-ray observations and with models. At bright knots observed by *IUE*, the B5 bandpass includes flux from several lines. However, supernova remnant (SNR) shock models imply that C IV λ1550 dominates for more typical conditions in SNRs, and *IUE* spectra demonstrate a strong correlation between C IV λ1550 flux and UIT B5 flux. The B5 image resembles images in [O III] λ5007, but to the east of the edge of the [O III] filaments there is a faint C IV emission, consistent with nonradiative shocked material behind the SNR blast wave. Conditions in shocked gases that lead to C IV emission are similar to those that produce [O III]. Hence the ratio of the B5 and [O III] intensities can be used to map the optical depths of the sheetlike regions that emit the C IV resonance line. A feature in the B5 emission closely follows a "bow shock" shape in *Einstein* HRI imagery; its morphology is consistent with an encounter of the SNR shock with a cloud outlined by a column density enhancement found in H I maps.

Subject headings: supernova remnants — ultraviolet: general

1. INTRODUCTION

The Cygnus Loop is the prototypical, middle-aged supernova remnant (SNR) (Raymond 1984). During the *Astro-1* mission the Ultraviolet Imaging Telescope (UIT) observed two positions on its northeastern shell. This *Letter* describes the results of UIT imagery of a 40′ diameter field centered at R.A. $20^h57^m30^s.5$, decl. 31°7′36″.8 (epoch 2000.0). Simultaneous observations were made with the Hopkins Ultraviolet Telescope (HUT) (Blair et al. 1991) and the Wisconsin Ultraviolet Photopolarimetry Experiment (Nordsieck et al. 1992). The UIT images are the first high-resolution UV imagery of the Cygnus Loop or similar evolved SNRs, and represent the first opportunity to compare wide-field UV observations of SNR shocks with other observations and with model predictions.

2. UIT IMAGES AND SPECTRAL CONTENT

Eight UIT frames of this field were made. The longest exposures in the near-UV (hereafter A1; 127 s; effective wavelength $\lambda_{\rm eff}$ for flat spectra = 2490 Å) and far-UV (hereafter B5; 1279 s; $\lambda_{\rm eff}$ = 1520 Å) are presented here. Descriptions of UIT and its operations, calibration, and data reduction are given in Stecher et al. (1992).

Figure 1*a* (Plate L3) shows the UIT B5 exposure, which strongly resembles ground-based ones made in [O III] λ5007 (see Fig. 3*b* [Pl. L4]). One important difference is the presence of faint emission to the east of the filaments in the UIT B5 image, which is absent even in deep [O III] images but appears in *Einstein* High-Resolution Imager (HRI) images (see Fig. 5 [Pl. L5]). This *Letter* is concerned primarily with the UIT B5 image and its comparison with visible- and X-ray–bandpass images.

Figure 1*b* shows the UIT A1 image, which resembles ground-based ones in Hα and other low-excitation lines. According to SNR models, many lines (C III] λ1909; C II] λ2326; [Ne IV] λ2423; Mg II λ2799) contribute to A1 flux; this complicates interpretation of the A1 image and probably causes its less-sharp appearance compared to B5.

2.1. *IUE Observations in the UIT Field*

UIT B5 fluxes were compared with those derived from *IUE* SWP spectra made within the field. UIT fluxes were computed by summing flux from the UIT image in an appropriately placed and oriented *IUE* aperture, minus a sky background. *IUE* spectra were integrated over the UIT B5 bandpass function and compared with the UIT results. For the 11 *IUE* SWP spectra in the field with exposure times longer than 250 minutes, the mean ratio of UIT to *IUE* flux for the B5 bandpass is 0.69 ± 0.27(σ), using the *IUE* calibration of Bohlin et al. (1990). This ratio is probably reduced by particle hits and made noisy by poor overall signal-to-noise ratio in the long *IUE* exposures. The equivalent ratio for the single HUT observations in the field is (UIT/HUT) = 1.29.

UV spectral observations of bright knots (Benvenuti, Dopita, & D'Odorico 1980; Raymond et al. 1980, 1981; Raymond et al. 1988, hereafter RHCBFG; Blair et al. 1991) show that the B5 bandpass includes significant flux from C IV λ1550 and O III] λ1666 as well as some N IV λ1485, He II λ1640, and N III] λ1745. For the brightest examples the O III] λ1666 UIT contribution is comparable to that of C IV, although reseau contamination is present in the 1660–1670 Å

[1] Hughes STX Corporation, Code 681, Goddard Space Flight Center, Greenbelt, MD 20771.
[2] Princeton University Observatory, Princeton, NJ 08544.
[3] Space Telescope Science Institute, Homewood Campus, Baltimore, MD 21218.
[4] Laboratory for Astronomy and Solar Physics, Code 680, Goddard Space Flight Center, Greenbelt, MD 20771.
[5] Astronomy Department, University of Virginia, P.O. Box 3818, Charlottesville, VA 22903.
[6] NASA Headquarters, Code M-6, Washington, DC 20546.
[7] National Radio Astronomy Observatory, Edgemont Road, Charlottesville, VA 22903.

1992ApJ...395L...9C

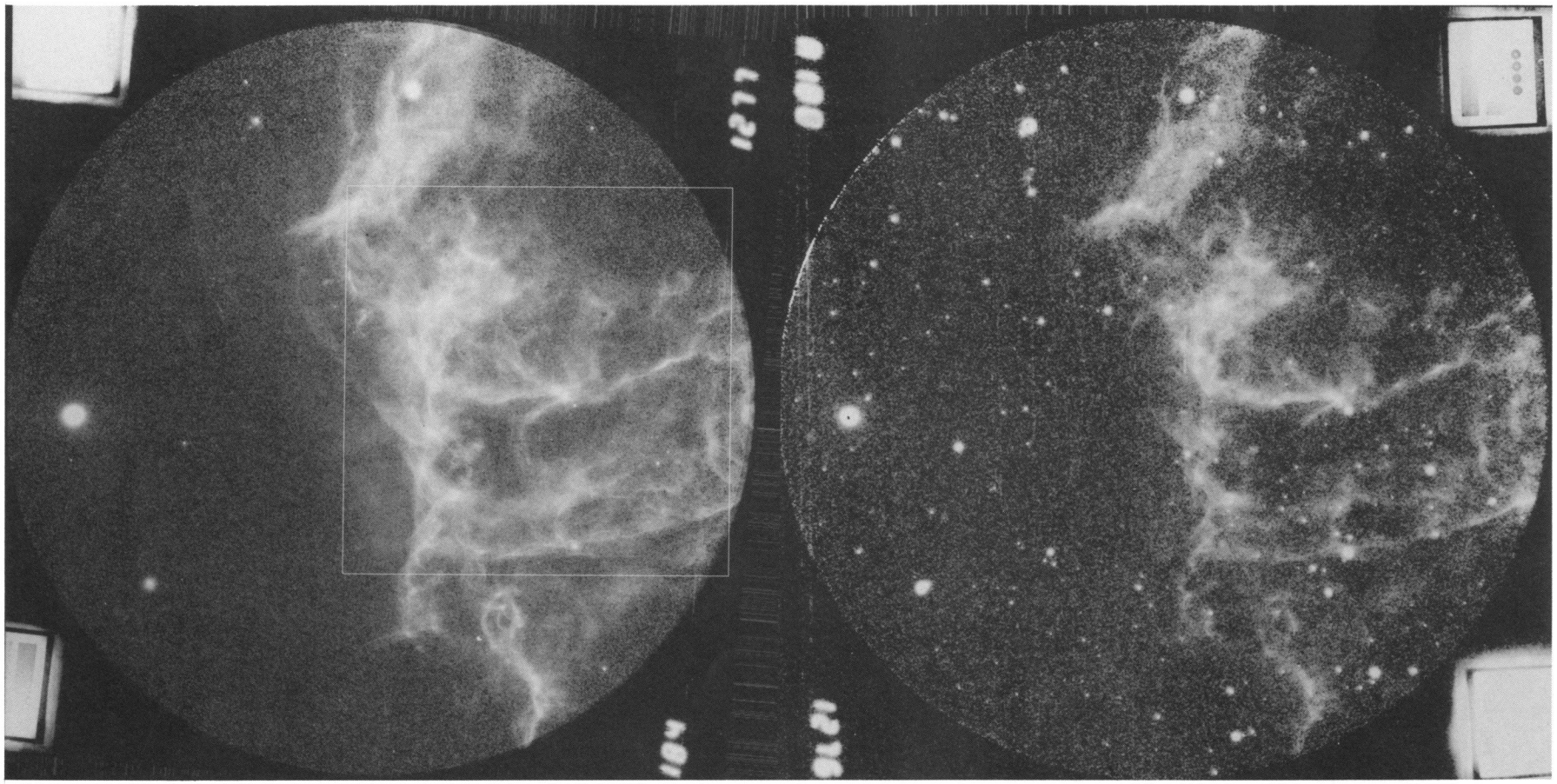

FIG. 1*a* FIG. 1*b*

FIG. 1.—(*a*) UIT's flat-fielded, linearized, and calibrated 1279 s B5 (far-UV) exposure, displayed with a logarithmic intensity function. North is at the top, east is to the left, and the field displayed is 40′ in diameter. The square outlines the field of view of Fig. 3. Other features discussed in the text are pointed out in Fig. 3*c*. (*b*) UIT's 127 s A1 (near-UV) exposure, displayed similarly to (*a*).

PLATE L4

FIG. 3*a*

FIG. 3*b*

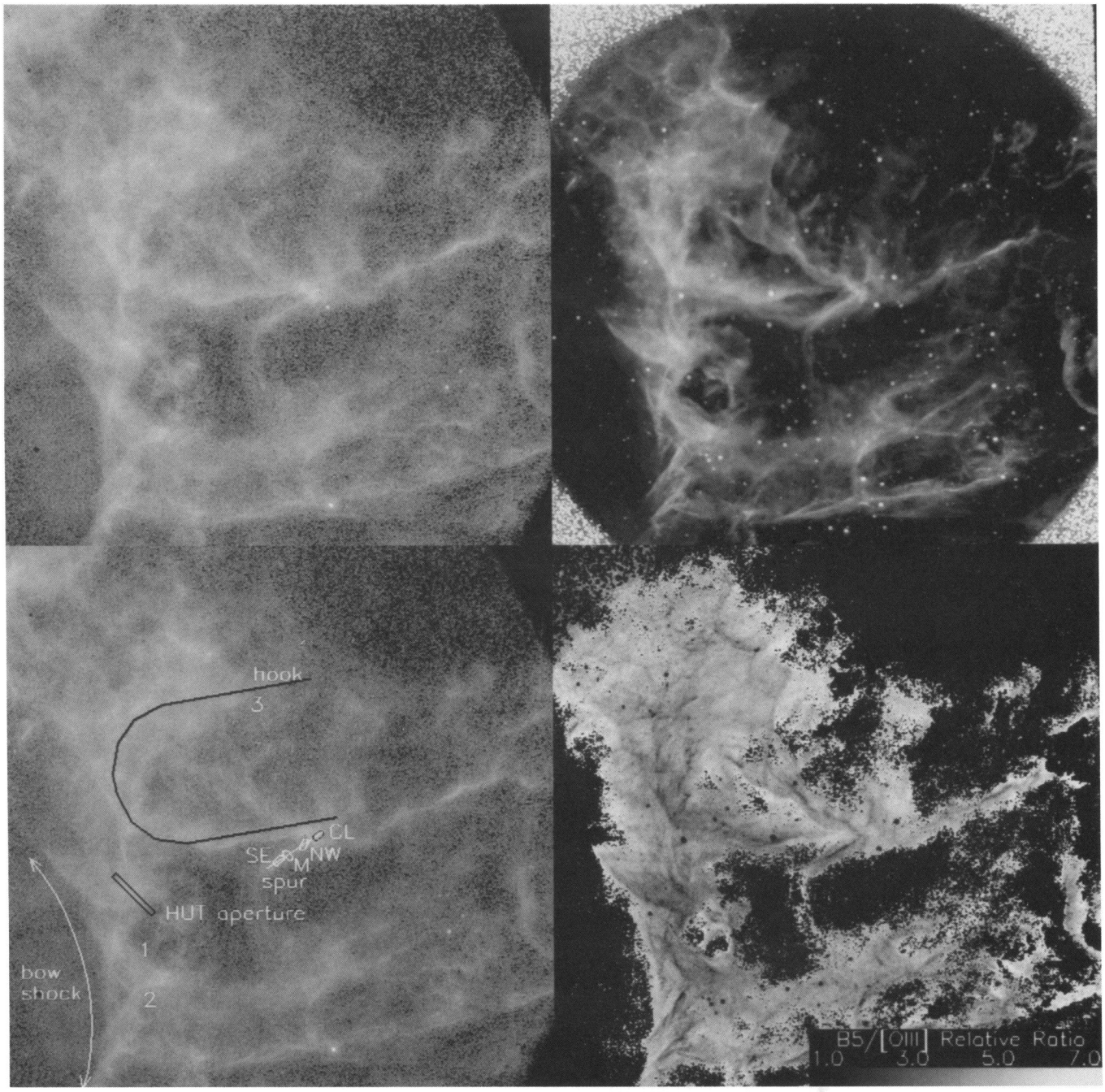

FIG. 3*c*

FIG. 3*d*

FIG. 3.—(*a*) A 20′ portion of the UIT B5 image, displayed with a logarithmic intensity function. (*b*) Ground-based image made in the 5007 Å [O III] line, geometrically corrected so that it is coaligned with (*a*) to within 4″ and scaled in intensity so that fluxes in (*a*) and (*b*) in the aperture marked "SE" (see [*c*]) are equal. The two images are scaled logarithmically in intensity in the same way, smoothed to resolutions of 3″–4″. (*c*) Image in (*a*) overlaid with the outline of the *IUE* apertures for positions SE, M, and NW of RHCBFG, as well as an *IUE*–sized aperture CL referred to in the text. The "spur" and the "hook," features at the positions marked 1, 2, and 3, and part of the apparent bow shock are marked; they are discussed in the text. The aperture for simultaneous observations by the Hopkins Ultraviolet Telescope is also outlined. (*d*) Ratio of the UIT B5 image to the [O III] image. Before division, the images were coaligned and smoothed to a resolution of about 4″; a flat sky flux was subtracted from each image, and pixels with values below "floors" representing S/N < 4 (for UIT) and S/N < 7 (for the [O III] image) for single pixels were masked off and are black in this figure. The gray scale at the bottom of the figure shows relative ratio as a function of gray value.

CORNETT et al. (see 395, L9 and L10)

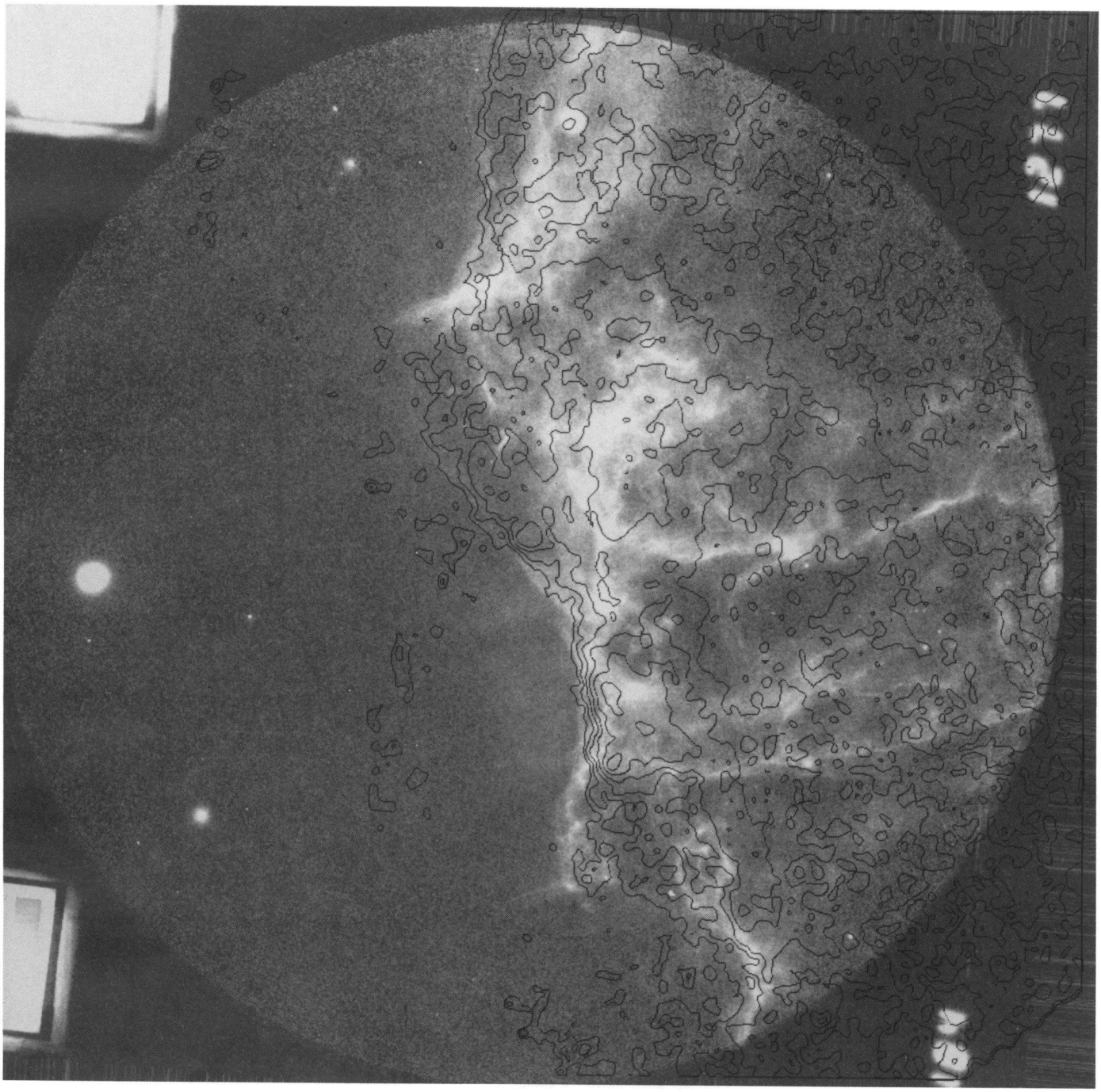

FIG. 5.—*Einstein* HRI X-ray contours superposed on a linearly displayed UIT B5 image; scale and orientation are the same as in Fig. 1. The HRI image was smoothed with a Gaussian filter of FWHM 19″ before contouring. Successive contour levels are in ratios of $\sqrt{2}$. Note the close correspondence of the X-ray and B5 intensity edges over 20′ along the "bow-shock" feature at the eastern edge of the remnant.

CORNETT et al. (see 395, L9 and L11)

wavelength range in all *IUE* spectra. In more typical locations, C IV λ1550 dominates the UIT bandpass, contributing more than twice the flux of any other spectral line. The behavior of O III] λ1666 and C IV is as expected: the C IV resonance line is intrinsically stronger, but, as column densities increase, the strength of the (collisionally excited) O III] line increases, while C IV λ1550 saturates due to the effects of resonance line scattering.

C IV flux as measured by *IUE* is strongly correlated with UIT B5 flux. C IV fluxes for the 11 *IUE* spectra used above were computed by summing flux in the 1540–1560 Å wavelength range, minus an estimated continuum background, and plotted against UIT B5 flux. A straight-line least-squares fit to the data has a slope of $0.94 \pm 0.05(\sigma)$, an intercept of 0.70 ± 0.83, and a correlation coefficient of 0.75. This relationship shows the usefulness of the UIT B5 flux as a measure of C IV λ1550 flux in this field.

2.2. *Model Predictions of Image Spectral Content*

We have used the models of Hartigan, Raymond, & Hartmann (1987, hereafter HRH) and Shull & McKee (1979) to predict contributions of spectral features in the B5 bandpass as a function of shock velocity. The models of HRH, while generated to predict parameters for regions of higher density than encountered here, produce the correct relative line intensities for the Cygnus region (J. C. Raymond, private communication). Models of HRH, Shull & McKee (1979), and others predict that line flux in UIT's B5 bandpass is significant only for shock velocities above 100 km s^{-1} and consists essentially of C IV λ1550 above that velocity. Relative flux from the two-photon continuum of hydrogen increases with shock velocity, equaling 50% of the C IV flux at about 300 km s^{-1} according to HRH.

Figure 2 displays the results of HRH for their model E (equilibrium preionization, preshock density 100 cm^{-3}). The relative fluxes in the UIT B5 filter for important components and the total model flux (the sum of all significant UV line and continuum fluxes) are shown. Model spectra have been reddened to $E(B-V) = 0.08$ (RHCBFG) using the reddening curve of Savage & Mathis (1979) and scaled by the relative B5 filter sensitivity as a function of wavelength.

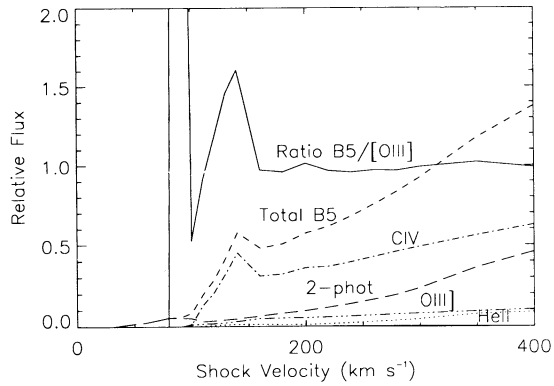

FIG. 2.—Predicted fluxes of interstellar shock models of Hartigan, Raymond, & Hartmann (1987). *Solid line:* Normalized ratio of total model flux in UIT B5 filter to [O III] λ5007 flux. Note that this ratio varies by relatively small amounts for velocities ($V_s > 100$ km s^{-1}) where there is significant B5 flux. *Short-dashed line*: Total model flux in UIT B5 filter. *Dot-dash line*: C IV λ1550 flux in UIT B5 filter. *Long-dashed line*: Hydrogen two-photon continuum flux in UIT B5 filter. *Dash-dot-dot-dot line*: O III] λ1665 flux in UIT B5 filter. *Dotted line*: He II λ1640 flux in UIT B5 filter. Model fluxes in UIT B5 filter are adjusted for relative filter response and reddening so that the plotted values are relative contributions to UIT B5 flux.

Applying shock models to observations is complicated by many effects. Chance superposition of features, multiple shock velocities, and geometrical effects in resonance lines (Raymond et al. 1981) contribute to uncertainties. Also, some shocks that are not modeled may strongly influence the relative contribution of two-photon continuum emission. Nonradiative shocks (Raymond et al. 1983) are strong emitters of He II λ1640 and C IV λ1550 but have weak two-photon continuum contributions, especially in the preionized case; incomplete shocks (RHCBFG) also have weaker two-photon contributions than the models predict. Finally, some of the B5 emission may be nearly pure two-photon emission from very slow ($V_s < 100$ km s^{-1}) shocks.

However, according to the models of HRH, UIT B5 images and ground-based [O III] λ5007 images observe material of similar excitation. The solid line in Figure 2 compares model results for the UIT B5 filter and [O III] λ5007. For shock velocities greater than 150 km s^{-1} the predicted ratio of B5 flux to [O III] flux varies by only a few percent; except for $V_s < 120$ km s^{-1}, where B5 and [O III] fluxes are small, the ratio as normalized varies between 1.0 and 1.6.

3. DISCUSSION

3.1. *The B5 Image and* [O III] *Data*

Figures 2 and 3*b* demonstrate the similar origins of B5 flux and [O III] λ5007 emission. However, the primary contributor to B5 flux, C IV emission, is a strong resonance line whose observed emission is often reduced by scattering in the line and consequent large optical depths (Raymond et al. 1981). [O III] λ5007 is a collisionally excited forbidden line which is never optically thick. This suggests a search for the effects of optical depth and saturation in C IV by comparing B5 and [O III] images in detail. For example, the ratio of B5 flux to [O III] flux should be large in regions where resonant scattering and optical depths have small effect, and vice versa. RHCBFG have studied C IV optical depth effects in the "spur" region by comparing observed *IUE* line ratios involving C IV λ1550 with models, and by delineating variations in the spatial structure of C IV emission. They conclude that C IV flux is attenuated by resonant scattering at the center and the southeast end of the spur, and less strongly at the northwest end.

UIT B5 data support this conclusion. Figure 3*a* (Plate L4) is a 20′ part of the UIT B5 image; Figure 3*b* is a coaligned [O III] λ5007 image. Figure 3*c* is identical to Figure 3*a* but has been overlaid with outlines of *IUE* apertures at the "SE," "M," and "NM" positions of RHCBFG, an *IUE*–sized aperture "CL" in the bright clump northwest of the end of the spur, and other features. The UIT image has been geometrically corrected to align with the [O III] image within 3″–4″, slightly larger than the UIT image's resolution; the [O III] image has been smoothed to 3.″4 resolution. In Figures 3*a* and 3*c* the UIT B5 image has been scaled so that aperture SE of RHCBFG in Figure 3*c* has the same apparent integrated brightness as the corresponding position in the [O III] image, in Figure 3*b*.

Position SE is relatively weak in C IV; the apertures marked "SE," "M," "NW," and "CL" have B5/[O III] ratios of 1.00, 0.95, 1.22, and 2.7, respectively, as scaled here. This implies that scattering effects cause a decrease in the C IV line intensity in the southeast end of the spur filament, in agreement with

FIG. 3*a*

FIG. 3*b*

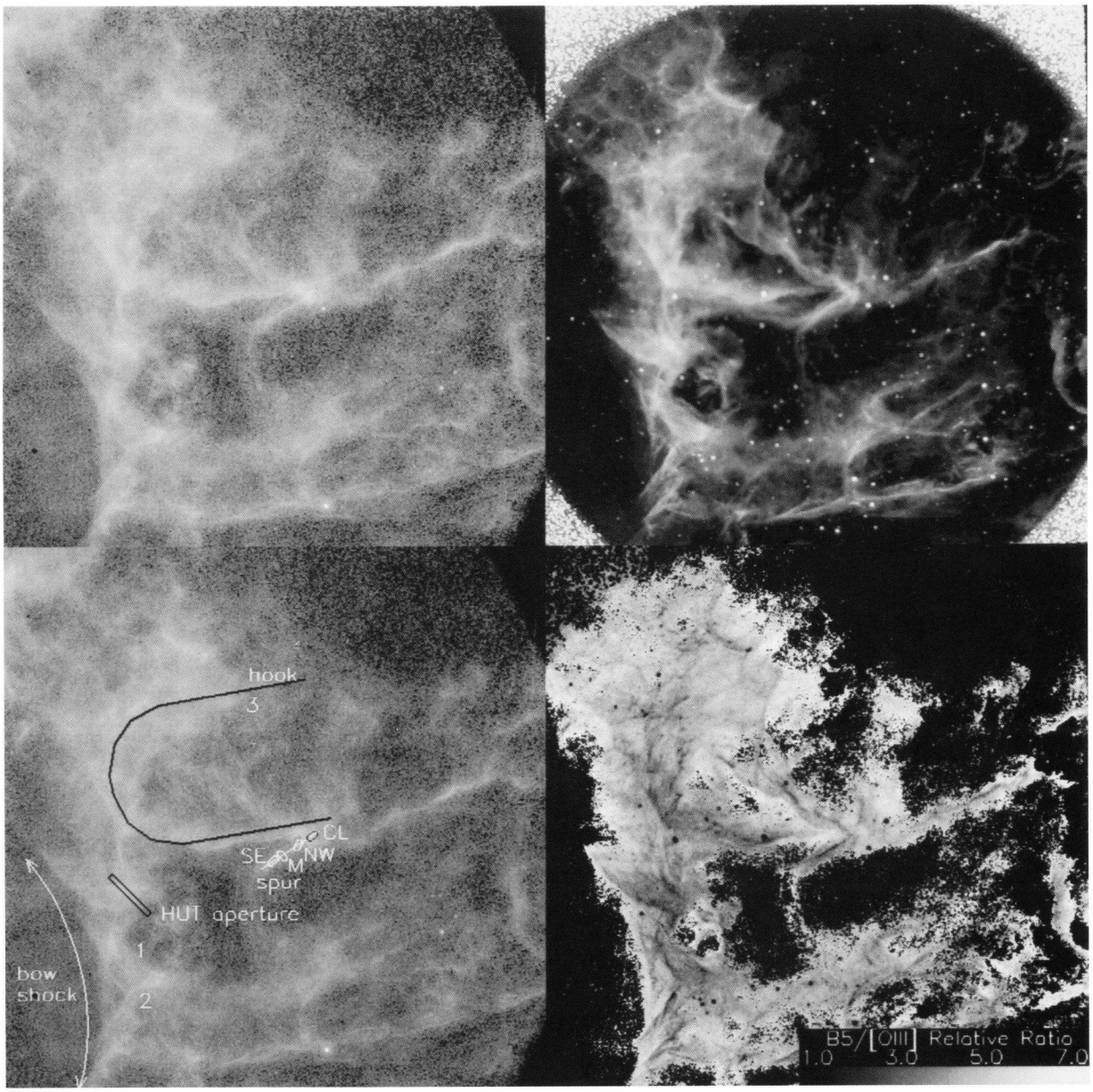

FIG. 3*c*

FIG. 3*d*

FIG. 3.—(*a*) A 20′ portion of the UIT B5 image, displayed with a logarithmic intensity function. (*b*) Ground-based image made in the 5007 Å [O III] line, geometrically corrected so that it is coaligned with (*a*) to within 4″ and scaled in intensity so that fluxes in (*a*) and (*b*) in the aperture marked "SE" (see [*c*]) are equal. The two images are scaled logarithmically in intensity in the same way, smoothed to resolutions of 3″–4″. (*c*) Image in (*a*) overlaid with the outline of the *IUE* apertures for positions SE, M, and NW of RHCBFG, as well as an *IUE*–sized aperture CL referred to in the text. The "spur" and the "hook," features at the positions marked 1, 2, and 3, and part of the apparent bow shock are marked; they are discussed in the text. The aperture for simultaneous observations by the Hopkins Ultraviolet Telescope is also outlined. (*d*) Ratio of the UIT B5 image to the [O III] image. Before division, the images were coaligned and smoothed to a resolution of about 4″; a flat sky flux was subtracted from each image, and pixels with values below "floors" representing S/N < 4 (for UIT) and S/N < 7 (for the [O III] image) for single pixels were masked off and are black in this figure. The gray scale at the bottom of the figure shows relative ratio as a function of gray value.

RHCBFG. The effect is smaller than that seen in comparisons of spectral measurements of C IV strength with model results because other emission (e.g., O III] λ1666 and two-photon continuum) contributes to the B5 bandpass, diluting optical depth effects.

Figure 3*d* is the ratio of the UIT B5 image to the [O III] image. Before division, a flat sky flux was subtracted from each image, and pixels with values below "floors" of good signal-to-noise ratio were masked off; masked-off pixels are black in this figure and generally lie outside the region of the filaments. Dark areas in filaments mark small ratios of B5/[O III] and therefore regions of large optical depth in C IV. Light areas denote large ratios and small optical depths. Because the B5 image has a smaller dynamic range than the [O III] image, owing to the smaller dynamic range of C IV emission, large C IV optical depths are selectively located at sharp [O III] features. Some remarkable examples are the spur filament and several of the sharper features (e.g., the ones marked 1 and 2 in Fig. 3*c*) at the east side of the [O III] emission. Small C IV optical depths are present in the diffuse material surrounding the sharper filaments, which may represent sheets of emitting material nearly normal to the line of sight. There are also notable regions of small C IV depth, including the one at "CL" (Fig. 3*c*), the diffuse east-west filament that is the end of the southern leg of the "hook," and the large diffuse region to the east of the knot marked 3 in Figure 3*c* as well as the knot itself. While multiple shock velocities and other complications are present, the pattern of relative B5 and [O III] intensities and B5/[O III] ratios is consistent with resonance line scattering due to large C IV optical depths as the primary cause.

Features like those at positions 1 and 2 in Figure 3*c* are characterized by a decrease in the C IV/[O III] ratio approaching scalloped arcs formed by [O III] rims. This suggests a geometrical explanation: large optical depths, due to resonant scattering in relatively narrow lines, are expected if sharp filaments are actually sheets of emitting material viewed nearly edge-on (Hester 1987). Conversely, amorphous clumps probably reflect chaotic velocity and spatial structure, broad lines, and small attenuation of C IV flux by resonant scattering.

This may be explored analytically for simple cases. We model a filament as the limb of a purely absorbing, expanding spherical shell of radius R. We approximate the velocity profile of the postshock emitting gas as a rectangle of width Δv and define the parameter $\tau_0 = nt/\Delta v$, where n is the volume density and t is the shell thickness, in units so that τ_0 is the true optical depth of the face-on shell material. In this case, the emission intensity from the shell may be expressed as a function of (l/R), where l is the projected distance from the sphere's center on the sky to the part of the shell being considered:

$$\frac{I(l/R)}{I(0)} = \left[1 - \left(\frac{l}{R}\right)^2\right]^{1/2} \frac{1 - e^{-\tau}}{1 - e^{-\tau_0}},$$

where $\tau = \tau_0[1 - (l/R)^2]^{-1}$. We expect $\tau_0 \ll 1$ for [O III] and $\tau_0 \sim 1$ for C IV (RHCBFG find $\tau = 0.5$ for a face-on shock in the spur from SNR models). In Figure 4 we plot $I(l/R)/I(0)$ for a range of values of τ_0; we also plot the ratio of $I(l/R; \tau_0 = 0.5)$ to $I(l/R; \tau_0 = 0.01)$, simulating the behavior of B5/[O III], to compare with Figure 3*c*. Although the three-dimensional geometry is uncertain, there are many locations in Figure 3*c* whose ratio profiles resemble this plot. (The apparent divergence for $l/R = 1$ is in fact relieved by the 1″ projected width of the cooling zone.)

This simple picture has potential complications. For example, the velocity width of the postshock gas may be determined by thermal Doppler broadening, which is an appreciable fraction ($\sim$0.5) of the maximum $\Delta v = V_s/4$ to be expected if emission from shocked material persists through cooling and recombination. If thermal broadening dominates, the above expression for intensity will revert to the usual curve-of-growth expressions for a saturated Gaussian profile, with optical depth replaced by $\tau_0/[1 - (l/R)^2]^{1/2}$.

3.2. *The B5 Image and Einstein HRI Data*

The Cygnus Loop is a well-known source of soft X-rays (Gorenstein et al. 1971). High spatial resolution observations (Ku et al. 1984, hereafter KKPL) are consistent with the "standard" picture of evolved SNRs: the X-ray emission apparently arises from a limb-brightened shell of hot gas produced by the expansion of a blast wave into an inhomogeneous interstellar medium. However, controversy remains over the relationship of regions of bright X-ray emission to optical filaments and density enhancements in the interstellar medium (Hester & Cox 1986, hereafter HC). The presence of coincident UV and X-ray emission east of the optical SNR's edge suggests using UIT images to study this relationship.

KKPL have observed the Cygnus Loop with HRI and Imaging Proportional Counter (IPC) instruments on the *Einstein Observatory*. HRI images, with 5″ resolution and energy range 0.15–4 keV, are well suited to comparison with UIT imagery. Figure 5 (Plate L5) shows *Einstein* HRI X-ray contours superposed on the UIT B5 image, which is displayed as in Figure 1. The HRI image was smoothed with a Gaussian filter of FWHM 19″ to reduce noise before contouring. Successive contours are in ratios of $\sqrt{2}$.

Viewed at coarse ($\sim$2′) resolution, several features correlate well, including the northeast end of the "hook" (see Fig. 3*c*), with the X-ray feature called "XC" by HC; the sharp eastern edge of HC's feature "XA" with an edge in the B5 image; and the highest X-ray contours with UV-bright knots in XA. The most remarkable correlation, however, is the sharp edge in both B5 and X-ray emission which extends beyond the northeast tip of a bright [O III] (and B5) filament near the field center. [O III] emission is restricted to the center 10′ of this edge; however, in both B5 and X-rays, the edge is twice that

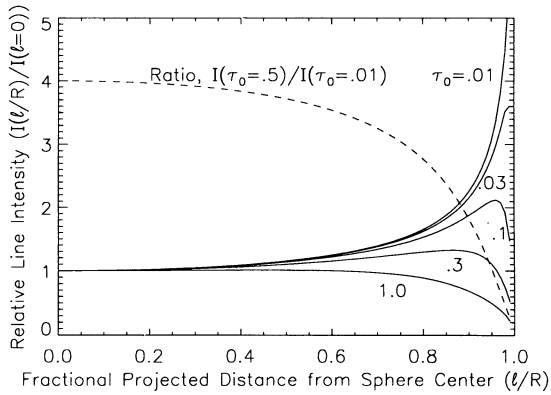

FIG. 4.—*Solid lines*: relative line emission intensity as a function of l/R, the projected distance in radii from the center of an expanding sphere with a rectangular velocity distribution profile. Plots are marked with values of τ_0, the face-on optical depth. *Dashed line*: relative ratio of the intensity for $\tau_0 = 0.5$ ($\sim$C IV) to the intensity for $\tau_0 = 0.01$ ($\sim$[O III]), which approximates the behavior of Fig. 2*c* across several bright filaments.

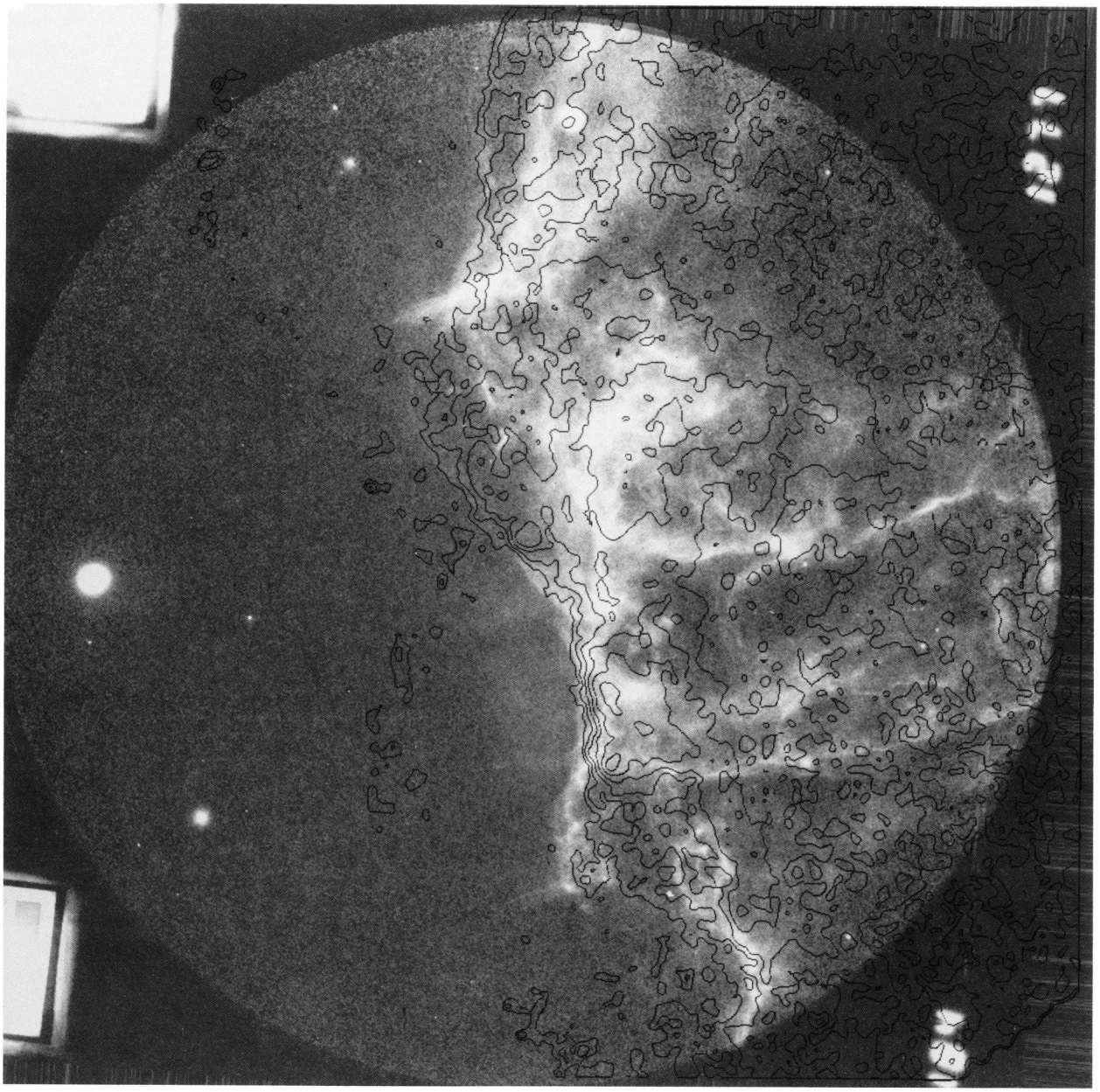

FIG. 5.—*Einstein* HRI X-ray contours superposed on a linearly displayed UIT B5 image; scale and orientation are the same as in Fig. 1. The HRI image was smoothed with a Gaussian filter of FWHM 19″ before contouring. Successive contour levels are in ratios of $\sqrt{2}$. Note the close correspondence of the X-ray and B5 intensity edges over 20′ along the "bow-shock" feature at the eastern edge of the remnant.

CORNETT et al. (see 395, L9 and L11)

long and forms a complete bow-shock shape. Faint B5 and fainter X-ray emission extend to the east past the sharp edge. This material is seen in very deep Hα images and in C IV, but not in very deep [O III] λ5007 images, and shows the signature of a nonradiative shock (Raymond et al. 1983).

This morphology reinforces the suggestion of HC that the enhanced X-ray emission at XA is caused by a reflected shock resulting from the collision of the blast wave with a cloud. Such a collision causes deceleration of the blast wave and pressure enhancement behind the blast wave; the increased pressure results in higher densities at a given temperature in the X-ray–emitting zone and enhanced X-ray emission.

The H I observations of DeNoyer (1975, Figs. 1*e* and 2) show an enhanced H I emission feature with a size and location consistent with the above interpretation, within the resolution limits of the H I observations (10′). The feature is at a radial velocity of 0–7 km s^{-1} compared with central velocity 33 km s^{-1} and expansion velocity 116 km s^{-1} for the Cygnus Loop measured by Minkowski (1958). Depending on the contours and geometry chosen to define the cloud, we compute sizes and densities in the range 5–10 pc and 10–20 cm^{-3}. In this interpretation, the coincident sharp edges of B5 and HRI emission mark the edge of the cloud; to the east there is a sharp transition from enhanced-pressure, doubly shocked (by the blast wave and subsequently the reflected shock) material to cold cloud material. Shocked material extends three-dimensionally from the apex in a paraboloid whose surface is seen edge-on at the sharp eastern edge of bright B5 and X-ray emission, and obliquely farther east as faint B5 emission, perhaps from a nonradiative shock. Nonradiative shocks are to be expected behind the blast wave near the X-ray boundaries of SNRs in recently overrun material.

The apparently coherent large feature described by the HRI and UIT images requires a longer time to form than the smaller one pointed out by HC. The size of the feature, as well as the faint B5 emission extending east from it, show the blast wave to have traveled 0.7 pc past the initial encounter with the cloud (about twice the result of HC), requiring 1700 yr at 400 km s^{-1}. This is considerably longer than the expected time for shocked cloud material to cool past the stage of strong [O III] emission, as pointed out by HC. It is therefore in apparent conflict with a simple geometrical model for the cloud-shock interaction, where one would expect to see progressive cooling stages represented by appropriate emission types (X-ray, C IV/[O III], Hα/[S II]) downstream from the shock front. However, even in the simple model proposed by HC and reinforced here, the material between the bow shock and the cloud has been shocked twice, and the precise location of the reflected shock front is not clear. Probably more important, the effects on X-ray, [O III], and C IV emission of the successive passing of a 400 km s^{-1} blast wave and a reflected shock of about half that velocity are uncertain.

UIT imagery provides a unique two-dimensional view of UV emission from SNRs. Further study of both the B5 and the A1 images may provide insight into the overall energetics of radiative shocks through comparison with *IRAS* and X-ray data; detailed comparison of the images with other optical-bandpass lines may provide the basis for studies of the three-dimensional structure of SNR filaments.

We thank Bill Blair for useful discussions and for providing us with the HUT spectrum in advance of its publication, and John Raymond for useful discussions and comments on an early draft. We thank Ron Angione and Fred Talbert for their help in obtaining the ground-based data. We are happy to acknowledge the Spacelab Operations Support Group at Marshall Space Flight Center and the *Astro-1* crew for their efforts before and during the mission.

REFERENCES

Benvenuti, P., Dopita, M., & D'Odorico, S. 1980, ApJ, 238, 601
Blair, W. P., et al. 1991, ApJ, 379, L33
Bohlin, R. C., Harris, A. W., Holm, A. V., & Gry, C. 1990, ApJS, 73, 413
DeNoyer, L. 1975, ApJ, 196, 479
Giacconi, R., et al. 1979, ApJ, 230, 540
Gorenstein, P., Harris, B., Gursky, H., Giacconi, R., Novick, R., & Vanden Bout, P. 1971, Science, 172, 369
Hartigan, P., Raymond, J. C., & Hartmann, L. 1987, ApJ, 316, 323 (HRH)
Hester, J. J. 1987, ApJ, 314, 187
Hester, J. J., & Cox, D. P. 1986, ApJ, 300, 675 (HC)
Ku, W. H.-M., Kahn, S. M., Pisarski, R., & Long, K. S. 1984, ApJ, 278, 615 (KKPL)
Minkowski, R. 1958, Rev. Mod. Phys., 30, 1058
Nordsieck, K., et al. 1992, in preparation
Raymond, J. C. 1984, ARA&A, 22, 75
Raymond, J. C., Black, J. H., Dupree, A. K., Hartmann, L., & Wolfe, R. S. 1980, ApJ, 238, 881
———. 1981, ApJ, 246, 100
Raymond, J. C., Blair, W. P., Fesen, R. A., & Gull, T. R. 1983, ApJ, 275, 636
Raymond, J. C., Hester, J. J., Cox, D., Blair, W. P., Fesen, R. A., & Gull, T. R. 1988, ApJ, 324, 869 (RHCBFG)
Savage, B. D., & Mathis, J. S. 1979, ARA&A, 17, 73
Shull, J. M., & McKee, C. F. 1979, ApJ, 227, 131
Stecher, T. P. 1992, ApJ, 395, L1